Fully relativistic *R*-matrix calculation of electron impact excitation of Ne IX

G. X. Chen,[1,2] R. K. Smith,[3,4] K. Kirby,[1,2] N. S. Brickhouse,[2] and B. J. Wargelin[2]
[1]*Institute for Theoretical Atomic, Molecular, and Optical Physics (ITAMP)*
[2]*Harvard-Smithsonian Center for Astrophysics, 60 Garden Street, Cambridge, Massachusetts 02138, USA*
[3]*Department of Physics and Astronomy, Johns Hopkins University, Baltimore, Maryland 21218, USA*
[4]*NASA Goddard Space Flight Center, Greenbelt, Maryland 20771, USA*
(Received 15 June 2006; published 9 October 2006)

We report on a fully relativistic close-coupling (CC) calculation of the electron impact excitation (EIE) of Ne IX. The multiconfiguration Dirac-Fock (MCDF) method was used in a calculation of Ne IX atomic structure. The EIE calculation of Ne IX was carried out using the Dirac *R*-matrix method and the MCDF orbitals for principal quantum number $n \leq 5$ with target states up to $n=5$ corresponding to 49CC (49 target states in the CC expansion). The EIE calculation included both resonance and channel coupling effects. We demonstrate that strong resonances appear in the excitation of the highly charged ion Ne IX, in particular for intercombination and forbidden transitions. Compared to less highly charged He-like ions, we show that for Ne IX all *N*-shell and *O*-shell levels start to give rise to Rydberg resonant states dipping just below *M*-shell and *N*-shell target thresholds, respectively. In comparison with previous calculations carried out with either the close-coupling or the distorted wave method, our calculations show significant differences with respect to cross sections and effective collision strengths. The important Ne IX line intensity *G* ratio ($G=(i+f)/r$=[forbidden +intercombination]/resonance) calculated based on our MCDF and Dirac *R*-matrix results is in good agreement with the existing accurate EBIT measurements. This calculation has direct applications to laboratory measurements and observations of astrophysical x-ray sources.

DOI: 10.1103/PhysRevA.74.042709 PACS number(s): 34.80.Kw, 95.30.Ky, 52.70.La

I. INTRODUCTION

Because of its stable heliumlike core, Ne IX appears over a wide range of astrophysical and laboratory plasma conditions [1–7]. X-ray lines from Ne IX can be used as important temperature, density, and abundance diagnostics for these plasmas. The importance of heliumlike systems in general, and Ne IX in particular, due to its large cosmic abundance, make an elaborate calculation of Ne IX, with an improved accuracy of relevant atomic processes, well worthwhile. In a collisional plasma, electron impact excitation (EIE) is one of the main mechanisms for populating the upper levels from which arise some important x-ray lines.

There are only a few previous calculations of EIE in Ne IX, mostly using the methods of Coulomb-Born (with exchange) and distorted wave (DW) [8,9]. However, the *R*-matrix (RM) method has also been used for the EIE calculation in Ne IX. The previous RM calculation for EIE in Ne IX was carried out in nonrelativistic *LS*-coupling followed by an algebraic transformation for the fine-structure transition collision strengths in [10]. Target states up to the principal quantum number $n=4$ (19 target terms corresponding to 31 fine-structure levels) were included in the close-coupling (CC) approximation in this study. Large differences were found in comparison with previous DW calculations. Very recently, another 31 target states CC calculation using the Breit-Pauli RM (BPRM) method was employed in the study of EIE in Ne IX [11]. Some major relativistic effects were included through the Breit-Pauli approximation.

There are several reasons to carry out an RM calculation from a purely atomic physics perspective. First, we extend the previous $n=4$ RM calculation to 49CC for target states up to $n=5$. This is necessary because the cascade effects from states up to $n=5$ (and possibly beyond) may make some contribution to the population for important Ne IX x-ray lines [5]. Second, in our treatment full relativistic effects are taken into account in both the target and the CC collision dynamics. Third, it is also necessary to check the accuracy of previous calculations by different methods (e.g., DW or CC), with respect to numerical details or physical effects, such as the resolution of Rydberg series of resonances and radiation damping effects.

Incentive for the present calculation is also provided by the recent experimental and observational studies of Ne IX. X-ray line intensity ratios in Ne IX have been measured in electron beam ion traps (EBIT) [3,7]. Prominent and strong lines of Ne IX have also been observed in x-ray spectra of the solar corona and other stellar coronae [1,2], and recently, in particular, from the solar-type star Capella (α Aurigae) using the Chandra X-ray Observatory (CXO) [6]. Ness *et al.* [6] found that the emission measure distribution (EMD) of Capella has a strong peak at electron temperature $T=6$ MK, indicating that the He-like Ne IX emission should originate from $T \approx 4-6$ MK; however, the *G* ratio formed from the $n=2 \rightarrow 1$ transitions ([forbidden + intercombination] / resonance) based upon earlier atomic calculations of Ne IX suggests $T \approx 2$ MK [6]. The present comprehensive calculation of improved Ne IX atomic data reduces this inconsistency and brings the measured *G* ratio into better (albeit not complete) agreement with other diagnostics, such as the thermal electron bremsstrahlung continuum. The quality of the x-ray spectra from these observations demands an improved and accurate calculation of atomic structure and EIE of Ne IX. With an appropriate atomic model such as the collisional radiative (CR) model employed in our work the atomic calculation and model with experimental calibration can be further used as an important tool for plasma diagnos-

tics. There are four lines contributing to the G ratio $[G \equiv (i+f)/r]$ corresponding to the following $n=2 \rightarrow 1$ transitions involving the K-shell $1s$ electron: (i) resonance w line (or r line) λ 13.447 Å: $1s^2\ ^1S_0 - 1s2p\ ^1P_1^o$; (ii) intercombination x line (or i line) λ 13.550 Å: $1s^2\ ^1S_0 - 1s2p\ ^3P_2^o$; (iii) intercombination y line (or i line) λ 13.553 Å: $1s^2\ ^1S_0 - 1s2p\ ^3P_1^o$; (iv) forbidden z line (or f line) λ 13.699 Å: $1s^2\ ^1S_0 - 1s2s\ ^3S_1$. The other $n=2 \rightarrow 1$ transitions ($1s^2\ ^1S_0 - 1s2s\ ^1S_0$ and $1s^2\ ^1S_0 - 1s2p\ ^3P_0^o$) are strictly forbidden. We report a G ratio based on our EIE calculation via an extensive CR model using the APEC code [5].

In this work, we employ the full relativistic Dirac R-matrix (DRM) method to calculate the EIE of Ne IX using the DARC codes [12]. The multiconfiguration Dirac-Fock (MCDF) GRASP2 code [13] is used for the target calculation for states up to the principal quantum number $n=5$. 49CC (49 target states in the CC expansion; hereafter mCC refers to m target states in the CC expansion) corresponding to target states up to $n=5$ are included in the EIE calculation. The methods and elaborate computational procedures used in this work have recently been applied to calculations of relativistic atomic structure and EIE of Fe XVII [14] and Ni XIX [15].

The paper is structured as follows. In Secs. II and III the basic theoretical and computational methods and techniques are sketched. In Sec. IV we present the results for cross sections and compare them with previous calculations. Our relativistic DW (RDW) code [16] was also used to calculate the related cross sections in order to compare with the backgrounds of the DRM cross sections. Based upon our DRM results, we also calculate a G ratio and compare it with results from previous calculations. In this section, we demonstrate that: (i) Dense resonance structure appears in some key transitions over the entire energy range below the highest threshold in the 49CC DRM collision strengths; indeed, resonance enhancement generally dominates forbidden and intercombination transitions; (ii) For Ne IX all N-shell and O-shell levels are starting to give rise to Rydberg resonant states dipping just below the M-shell and N-shell target thresholds, respectively. (iii) Our computed G ratios agree with EBIT measurements [3] to 8% (the uncertainty in EBIT measurements [3]). The conclusions are summarized in Sec. V.

II. THEORY

We use the N- and $(N+1)$-electron Dirac-Coulomb (DC) Hamiltonian to describe the target and the collisional atomic system, respectively. The DC Hamiltonian in Rydberg units for electrons i and j in a central field Z (atomic number $Z=10$ for Ne IX) can be written as

$$H^{\mathrm{DC}} = \sum_{i=1} \left(\boldsymbol{\alpha} \cdot \boldsymbol{p}_i/\alpha + \beta/\alpha^2 - \frac{2Z}{r_i} + \sum_{j>i} \frac{2}{r_{ij}} \right); \qquad (2.1)$$

where the quantities $\boldsymbol{\alpha}$ and β are the Dirac matrices in the low-energy representation and $\alpha = 1/137.036$ is the fine-structure constant. The total wave functions for a given symmetry $J\pi$ (J is the total angular momentum in a jj-coupling scheme and π is the parity) are constructed from bound $[\phi_{n\kappa m}(\boldsymbol{r})]$ and free $[\theta_{\epsilon\kappa m,i}(\boldsymbol{r})]$ Dirac four-component spinors

$$\phi_{n\kappa m}(\boldsymbol{r}) = \langle r | n\kappa m \rangle = \frac{1}{r} \begin{bmatrix} P_{n\kappa}(r) & \chi_{\kappa m}(\boldsymbol{r}/r) \\ iG_{n\kappa}(r) & \chi_{-\kappa m}(\boldsymbol{r}/r) \end{bmatrix}, \qquad (2.2)$$

$$\theta_{\epsilon\kappa m,i}(\boldsymbol{r}) = \langle r | \epsilon\kappa m, i \rangle = \frac{1}{r} \begin{bmatrix} F_{\epsilon\kappa,i}(r) & \chi_{\kappa m}(\boldsymbol{r}/r) \\ iQ_{\epsilon\kappa,i}(r) & \chi_{-\kappa m}(\mathbf{r}/r) \end{bmatrix}, \qquad (2.3)$$

where the real and imaginary radial Pauli spinors are the large and small component, respectively (i represents the index of continuum bases used for a free radial spinor with a continuum orbital energy ϵ). The function $\chi_{\kappa m}$ is the spinor spherical harmonic

$$\chi_{\kappa m}(\boldsymbol{r}/r) = \sum_{\sigma=\pm\frac{1}{2}} \left\langle lm - \sigma \tfrac{1}{2} \sigma \middle| l \tfrac{1}{2} jm \right\rangle \mathrm{Y}_l^{m-\sigma}(\vartheta, \varphi) \phi^{\sigma}, \qquad (2.4)$$

where $\langle lm - \sigma\frac{1}{2}\sigma | l\frac{1}{2} jm \rangle = C(lm - \sigma\frac{1}{2}\sigma; jm)$ is a Clebsch-Gordan coefficient, $\mathrm{Y}_l^{m-\sigma}(\vartheta, \varphi)$ is a spherical harmonic, ϕ^{σ} a spinor basis function, and κ the relativistic angular quantum number $\kappa = -(j+1/2)a$ for $l = j - 1/2a$ $(a = \pm 1)$, thus $j = |\kappa| - 1/2$. m and σ are the magnetic quantum numbers along some arbitrary projection axis for the orbital angular momentum l and the spin of the bound or free electron, respectively.

The radial functions satisfy orthonormality conditions

$$\int_0^{R_0} \mathrm{d}r [P_{n\kappa}(r) P_{n'\kappa}(r) + Q_{n\kappa}(r) Q_{n'\kappa}(r)] = \delta_{nn'}, \qquad (2.5)$$

$$\int_0^{R_0} \mathrm{d}r [F_{\epsilon\kappa,i}(r) F_{\epsilon'\kappa,i'}(r) + G_{\epsilon\kappa,i}(r) G_{\epsilon'\kappa,i'}(r)] = \delta(\epsilon - \epsilon') \delta_{ii'}, \qquad (2.6)$$

where R_0 is the boundary of the Dirac R-matrix (DRM) inner region.

The atomic structure is calculated by the MCDF method which is a self-consistent-field procedure, in which both the orbitals and the configuration expansion coefficients are variationally determined. The GRASP2 code with slight modifications was used for the target calculation [13]. For a target so specified, electron collision processes are described using a partial-wave (PW) expansion with radial functions satisfying the $(N+1)$-electron DC Hamiltonian in Eq. (2.1), leading to close-coupling (CC) solutions. Using the PW approach for the colliding electron, the coupled-channel wave function expansion for the $(e+\mathrm{Ne\ IX})$ system may be expressed

$$\Psi(E; e + \mathrm{Ne\ IX}) = \sum_i \chi_i(\mathrm{Ne\ IX}) \theta_{\mathrm{e},i}(\kappa) + \sum_j c_j \Phi_j(\mathrm{Ne\ VIII}), \qquad (2.7)$$

where Ψ denotes the continuum $(E>0)$ states of a given symmetry $J\pi$, expanded in terms of the core ion eigenfunctions $\chi_i(\mathrm{Ne\ IX})$ with a specific total angular momentum and parity combination $J_\iota \pi_\iota$ of the target, and the PW $\theta_{\mathrm{e},i}(\kappa)$ for the colliding electron $(N+1)$ (with relativistic quantum number κ_ι) in a channel labeled $J_\iota \pi_\iota\ k_\iota \kappa_\iota [J\pi]$; k_ι^2 is the channel

energy in Rydbergs (<0 if closed, 1 Ry=13.6059 eV). The variationally added functions Φ_j(Ne VIII), sometimes referred to as "bound channels" as opposed to the continuum or "free" channels in the first sum over the target states, form a set of L^2-integrable antisymmetrized wave functions for the $(N+1)$-electron system. They are products of $(N+1)$ target orbitals, included (a) to compensate for loss when orthogonalizing the continuum with bound orbitals; and (b) to add short-range correlation, often of crucial importance in scattering and radiative CC calculations. Orthogonality is imposed for convenience in order to avoid cumbersome overlap integrals in the Hamiltonian matrix and possible instabilities in numerical procedures. The DRM is used to find the unknown radial functions $\theta_{e,i}(\kappa)$ and coefficients c_j in Eq. (2.7). Dirac *R*-matrix DARC codes with some modifications were used to carry out the collision calculation [12].

III. COMPUTATIONS

A. Target eigenfunctions

The Ne IX target wave functions up to $n=5$ and relativistic angular quantum number $|\kappa|$ up to 5 (or the total angular momentum j up to 9/2) for the singly excited electron from the $1s$ shell are calculated using the multiconfiguration Dirac-Fock (MCDF) method [*N*-electron DC Hamiltonian in Eq. (2.1)]. An expansion over the 15 configurations $1s^2$, $1s2s$, $1s2p$, $1s3s$, $1s3p$, $1s3d$, $1s4s$, $1s4p$, $1s4d$, $1s4f$, $1s5s$, $1s5p$, $1s5d$, $1s5f$,$1s5g$ yields 29 *LS terms* and 49 fine-structure *levels*. Target energies from the MCDF code GRASP2 for this set of configurations are compiled in Table I and compared with observation. Selected multipole transition probabilities for the transitions among target states are compared with other work in Table II.

B. Electron impact excitation

The DRM calculation is briefly described below. In jj collisional coupling the target levels add up to symmetries $J\pi$ of coupled integrodifferential equations that reach their maximum of complexity at 9/2 (odd parity) with 216 free channels and 107 bound channels [Φ_j(Ne VIII)] and one arrives at a Hamiltonian matrix of size 8747×8747 when expanding each PW with 40 continuum orbitals in the inner region—just enough to allow electron-impact energies ϵ up to 160 Ry (the ionization potential of Ne IX is 87.891 Ry) at an *R*-matrix boundary of $R_0=10.4a_0$ (where $5s$, the most diffuse target orbital, is tailing off with magnitude 0.0020). The DRM method calculates CC collision strengths Ω for all values $J\leq 81/2$ for both the odd and even parities, comprising PW in the range $|\kappa|=1-46$. This ensures PW convergence of the collision strengths in the low-energy region, which may be characterized by resonance features. In the smooth high-energy region procedures known as "PW top-up" are used to include higher partial waves [17]. Special attention is paid to convergence with respect to resolving resonances. We use a constant-energy mesh of up to 56 000 energies to compute effective collision strengths for practical applications.

A useful tool when assessing collision strengths is the Burgess-Tully plot [18] of reduced collision strength versus reduced collision energy. This approach has been used in our previous calculation of Fe XVII [17,19]. The same approach is used in the present work to calculate the effective collision strengths.

C. Effective collision strength

The procedure for obtaining the effective collision strength $\Upsilon(T)$ [i.e., the Maxwellian-averaged collision strength $\Omega(E_i)$] can be found in our earlier publications [17]. This quantity for the transition from the initial state i to the final state "f" is defined

$$\Upsilon_{if}(T)=\int_{\Delta E_{if}}^{\infty}\Omega_{if}(E_i)e^{-E_i/k_BT}d(E_i/k_BT), \tag{3.1}$$

where ΔE_{if} is the transition energy between levels i and f. The expression for the cross section, $\sigma_{if}(E_i)$, for a transition $i\rightarrow f$ in terms of the collision strength $\Omega_{if}(E_i)$, a dimensionless symmetric quantity ($\Omega_{if}=\Omega_{fi}$) is,

$$\sigma_{if}(E_i)=\frac{\pi a_0^2}{k_i^2 g_i}\Omega_{if}(E_i), \tag{3.2}$$

where k_i is a pure number measuring the waves of the impact electron across the length of a Bohr radius a_0. It is related to its kinetic energy E_i by

$$k_i^2=E_i+\frac{\alpha^2E_i^2}{4}. \tag{3.3}$$

Then the rate coefficient $q_{if}(T)$ can be written

$$q_{if}(T)=\frac{8.629\times 10^{-6}\ \mathrm{cm^3\ s^{-1}}}{\sqrt{T/\mathrm{K}}}\frac{\Upsilon_{if}(T)}{g_i}\exp\left(-\frac{\Delta E_{if}}{k_BT}\right), \tag{3.4}$$

where $k_B=1.380\,651\cdot 10^{-16}$ erg/K is the Boltzmann constant and g_i is the statistical weight of the initial state i.

IV. RESULTS AND DISCUSSION

In this section we report on the results of our atomic structure calculation of Ne IX using the MCDF method. The MCDF orbitals are further used in the EIE calculation of Ne IX both with the DRM method and the RDW method [16]. Our RDW results are compared with the backgrounds of the DRM cross sections in order to elucidate the channel coupling effects. We also compare our calculation of collision strengths and effective collision strengths with previous calculations.

A. Target energies

The calculated energies in Table I from GRASP2 are compared with observed values where available. Moreover Table I provides the key when assigning levels by number to quantities for radiative or collisional transitions. The computations tend to overestimate the binding energy of the ground

TABLE I. The 49 fine-structure levels up to $n=5$ and their calculated and observed energies E in Rydbergs for Ne IX. Observed values are from NIST [22]; MCDF are from GRASP2 calculations. The index i is used as a shorthand to label the levels. n.b. both jj-coupling and LS-coupling notation are given for the level designations of Ne IX.

i	SLJ	jj	E(MCDF)	E (observed)
1	$1s^2\ ^1S_0$		0.0	0.0
2	$1s2s\ ^3S_1$	(1/2,1/2)1	66.51725	66.52195
3	$1s2p\ ^3P^o_0$	$(1/2,1/2)^o0$	67.23377	67.23511
4	$1s2p\ ^3P^o_1$	$(1/2,1/2)^o1$	67.23717	67.23784
5	$1s2p\ ^3P^o_2$	$(1/2,3/2)^o2$	67.25249	67.25197
6	$1s2s\ ^1S_0$	(1/2,1/2)0	67.32429	67.27593
7	$1s2p\ ^1P^o_1$	$(1/2,3/2)^o1$	67.81898	67.76692
8	$1s3s\ ^3S_1$	(1/2,1/2)1	78.59418	78.57856
9	$1s3p\ ^3P^o_0$	$(1/2,1/2)^o0$	78.78781	78.77357
10	$1s3p\ ^3P^o_1$	$(1/2,1/2)^o1$	78.78899	78.77448
11	$1s3s\ ^1S_0$	(1/2,1/2)0	78.79364	78.77795
12	$1s3p\ ^3P^o_2$	$(1/2,3/2)^o2$	78.80409	78.77867
13	$1s3d\ ^3D_1$	(1/2,3/2)1	78.90251	78.88839
14	$1s3d\ ^3D_2$	(1/2,3/2)2	78.90277	78.88948
15	$1s3d\ ^3D_3$	(1/2,5/2)3	78.90412	78.89012
16	$1s3d\ ^1D_2$	(1/2,5/2)2	78.91071	
17	$1s3p\ ^1P^o_1$	$(1/2,3/2)^o1$	78.94829	78.92056
18	$1s4s\ ^3S_1$	(1/2,1/2)1	82.71749	82.69931
19	$1s4p\ ^3P^o_0$	$(1/2,1/2)^o0$	82.79647	82.77950
20	$1s4p\ ^3P^o_1$	$(1/2,1/2)^o1$	82.79700	82.77987
21	$1s4s\ ^1S_0$	(1/2,1/2)0	82.79900	82.78005
22	$1s4p\ ^3P^o_2$	$(1/2,3/2)^o2$	82.80221	82.78160
23	$1s4d\ ^3D_1$	(1/2,3/2)1	82.84347	82.83691
24	$1s4d\ ^3D_2$	(1/2,3/2)2	82.84360	82.83728
25	$1s4d\ ^3D_3$	(1/2,5/2)3	82.84415	82.83773
26	$1s4f\ ^3F^o_3$	$(1/2,5/2)^o3$	82.84676	
27	$1s4f\ ^3F^o_2$	$(1/2,5/2)^o2$	82.84685	
28	$1s4f\ ^3F^o_4$	$(1/2,7/2)^o4$	82.84720	
29	$1s4f\ ^1F^o_3$	$(1/2,7/2)^o3$	82.84732	
30	$1s4d\ ^1D_2$	(1/2,5/2)2	82.84774	
31	$1s4p\ ^1P^o_1$	$(1/2,3/2)^o1$	82.86266	82.83992
32	$1s5s\ ^3S_1$	(1/2,1/2)1	84.60429	84.58563
33	$1s5p\ ^3P^o_0$	$(1/2,1/2)^o0$	84.64401	84.62609
34	$1s5p\ ^3P^o_1$	$(1/2,1/2)^o1$	84.64430	84.62628
35	$1s5p\ ^3P^o_2$	$(1/2,3/2)^o2$	84.64534	84.62719
36	$1s5s\ ^1S_0$	(1/2,1/2)0	84.64679	84.62618
37	$1s5d\ ^3D_1$	(1/2,3/2)1	84.66775	84.64304
38	$1s5d\ ^3D_2$	(1/2,3/2)2	84.66783	84.64304
39	$1s5d\ ^3D_3$	(1/2,5/2)3	84.66810	84.64304
40	$1s5f\ ^3F^o_3$	$(1/2,5/2)^o3$	84.66957	84.65489
41	$1s5f\ ^3F^o_2$	$(1/2,5/2)^o2$	84.66961	
42	$1s5f\ ^3F^o_4$	$(1/2,7/2)^o4$	84.66979	84.65489
43	$1s5g\ ^3G_4$	(1/2,7/2)4	84.66982	
44	$1s5g\ ^3G_3$	(1/2,7/2)3	84.66985	
45	$1s5f\ ^1F^o_3$	$(1/2,7/2)^o3$	84.66986	
46	$1s5g\ ^3G_5$	(1/2,9/2)5	84.66997	
47	$1s5g\ ^1G_4$	(1/2,9/2)4	84.66999	

TABLE I. (*Continued.*)

i	*SLJ*	*jj*	*E*(MCDF)	*E* (observed)
48	$1s5d\ ^1D_2$	(1/2,5/2)2	84.67012	
49	$1s5p\ ^1P^o_1$	(1/2,3/2)°1	84.67766	

state by about 47 mRy, which is of no consequence when applied to collision work. Assigning intermediate coupling labels can be done from target *SLJ* eigenvectors as long as one component heavily dominates, but fails if level splitting within a term becomes comparable to term energy separations.

B. Transition probabilities

We present a *selection* of calculated radiative transition probabilities *A* (s^{-1}) in Table II. All the transitions shown in Table 2 in [10] and the NIST table [22] are also presented in our Table II for the purpose of convenient comparisons with the NIST evaluated and recommended values and previous calculations using the configuration-interaction (CI) approach with relativistic corrections [10]. The *A* coefficients calculated by many-body perturbation theory (MBPT) are also shown for comparison [23]. In Table II transition probabilities for both direct and spin-flip [or intercombination (IC)] dipole allowed E1 transitions, and some higher multipole transitions are collected, probing the quality of the target representation, which is crucial in the collisional applica-

TABLE II. Comparison of transition probabilities, *A* (in s^{-1}), for selected Ne IX transitions, for the present MCDF calculation, previous MBPT calculations, and measurements. The index *i* and *j* label the levels involved in the transition from levels *i* to *j* (see Table I).

i	*j*	Type	*A*(MCDF)	*A*(CI) [10]	*A*(NIST) [22]	*A*(MBPT) [23]
2	1	M1 (*z*)	9.81×10^{3}[a]			1.092×10^{4}
4	1	IC (*y*)	4.58×10^{9}			5.253×10^{9}
5	1	M2 (*x*)	2.21×10^{6}			2.257×10^{6}
7	1	E1 (*w*)	9.17×10^{12}	9.15×10^{12}	8.87×10^{12}	8.853×10^{12}
8	1	M1	4.01×10^{3}			
10	1	IC	1.71×10^{9}			1.604×10^{9}
11	1	M2	7.97×10^{5}			
13	1	M1	3.83×10^{1}			
14	1	E2	1.79×10^{7}			
15	1	M3				
16	1	E2	6.31×10^{8}			
17	1	E1	2.66×10^{12}	2.95×10^{12}	2.48×10^{12}	2.478×10^{12}
3	2	E1	1.03×10^{8}	9.59×10^{7}	9.80×10^{7}	
4	2	E1	1.05×10^{8}	9.93×10^{7}	9.80×10^{7}	
5	2	E1	1.12×10^{8}	1.07×10^{8}	9.80×10^{7}	
6	2	M1	9.28×10^{-2}			
7	2	IC	2.90×10^{5}			
9	2	E1	1.45×10^{11}	1.43×10^{11}	1.460×10^{11}	
10	2	E1	1.45×10^{11}	1.43×10^{11}	1.460×10^{11}	
12	2	E1	1.44×10^{11}	1.43×10^{11}	1.460×10^{11}	
13	3	E1	2.44×10^{11}	2.42×10^{11}	2.433×10^{11}	
13	4	E1	1.83×10^{11}	1.81×10^{11}	1.825×10^{11}	
14	4	E1	3.23×10^{11}	3.18×10^{11}	3.285×10^{11}	
13	5	E1	1.22×10^{10}	1.20×10^{10}	1.218×10^{10}	
14	5	E1	1.07×10^{11}	1.04×10^{11}	1.095×10^{11}	
15	5	E1	4.39×10^{11}	4.33×10^{11}	4.380×10^{11}	
7	6	E1	3.62×10^{7}	3.88×10^{7}	3.29×10^{7}	
17	6	E1	1.42×10^{11}	1.51×10^{11}	1.400×10^{11}	
16	7	E1	4.10×10^{11}	4.09×10^{11}	4.180×10^{11}	

[a]The small *A* coefficient for this *z* line from the recent EBIT measurements is $(1.105\pm0.018)\times10^{4}$ s^{-1} [20] and $(1.090\pm0.005)\times10^{4}$ s^{-1} [21].

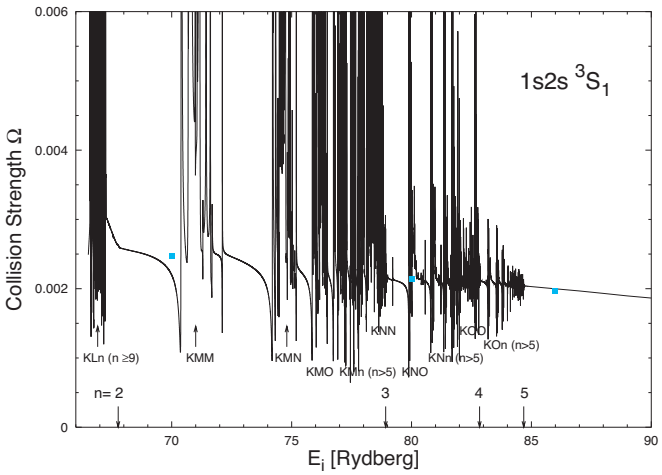

FIG. 1. (Color) Collision strength Ω from $n=5$ DRM calculations with detailed resonance structures as a function of incident electron energy E_i for M1 transition $1s^2\ ^1S_0-1s2s\ ^3S_1$. The green squares are our RDW values [16]. The down arrows mark the target threshold for each n complex. The major resonance complexes, with n being the principal quantum number of the third electron, are identified (see text for more discussions).

tion. Generally, the present MCDF A coefficients are in agreement with those in [10], although our A coefficients are in better agreement with NIST and MBPT values. Thus we may have a slightly better target than [10] for further EIE calculations.

We also present in Table II the transition probabilities for x-ray lines w, x, y, z in particular. Although some transitions have small rates, the lines themselves can be very strong due to EIE with strong resonances and cascade effects, depending on the plasma conditions.

C. Electron impact excitation of Ne IX

1. Resonant transitions (focusing on the w, x, y, z transitions)

Figure 1 shows extensive resonances in the collision strength for the transition from the ground state to the first excited state, $1s2s\ ^3S_1$, which gives rise to a forbidden (magnetic dipole, M1) transition. The dominant role of resonances is clear when contrasted with the background collision strengths obtained from the RDW calculations, which give only the nonresonant background. The down arrows mark the thresholds of $n=2$, 3, 4, 5 target states, respectively—the $n=5$ threshold corresponds to the highest target energy in our 49CC DRM calculation. The RDW collision strengths were computed using our RDW code [16]. The up arrows mark the Rydberg series of resonances which converge from below onto each of the $n=2$, 3, 4, 5 target thresholds, respectively. It is seen clearly that dense resonance complexes appear in the incident energies below the $n=3$ target threshold. The resonance enhancement decreases for E_i spanning the higher $n=4$ and 5 states. There is some small but significant resonance enhancement between the thresholds of $n=4$ and 5. It is expected that the interacting Rydberg series of resonances due to higher target states ($n>5$) should not have significant contribution to the collision rates. The resonance complexes KMM, KMN, and KMO, etc., can be clearly discerned in this figure. The more crowded and dense resonance complexes are marked with KLn ($n\geq 9$), KMn ($n>5$),KNn ($n>5$), and KOn ($n>5$).

We note a particular feature in this plot: KNN and KOO resonance complexes dip from above to just below the M- and N-shell thresholds, respectively. From the previous EIE study of Fe XVII, we have demonstrated similar behavior in that all N-shell levels give rise to Rydberg resonant states dipping below all M-shell thresholds [17]. With increasing effective nuclear charge $z_{\rm eff}=Z-2$ for He-like isoelectronic sequence, Ne IX is the first He-like ion for which higher $n+1$ resonance complexes dip from above into n target thresholds if $n\leq 4$ as shown in the present 49CC close coupling calculation. Inclusion of N-shell configurations $n=4$ leads to Rydberg resonance series, modifying the resonance pattern below the $n=3$ thresholds by its lowest-lying members, which can result in a fairly broad resonance structure. However, unlike the case study of 89CC ($n=4$) EIE calculation of Fe XVII where such features strongly modify 37CC ($n=3$) collision strengths down to every excitation threshold, not merely over the extended target energy range, the influence of this feature in EIE of Ne IX on the Maxwellian averaged effective collision strengths is still rather small because only one member of the series of resonance complexes (i.e., KNN or KOO) shows this "below-threshold" behavior.

With increasing $z_{\rm eff}$, we expect many more levels to be excited, as the n complexes become more degenerate, and more bound states and autoionizing resonances can be formed with the corresponding excited levels as parent or core states. The energy difference between the parent level and the bound electron increases as $z_{\rm eff}^2$, and therefore the autoionizing resonances for a given n appear at lower energies. Further study of higher $z_{\rm eff}$ He-like ions is ongoing to explore this interesting finding.

We discuss in particular the RDW results as representative of a long string of previous calculations in the literature using distorted-wave (DW) approximations, the Coulomb-Born (CB) approximation, or their variants [8,9]. Our RDW values agree well with the background of the present DRM collision strengths. The RDW calculations include relativistic and correlation effects, but do not allow for the channel coupling effects and resonance features. The RDW method may be thought of as a 2CC calculation including initial and scattered channels, without the remaining channel coupling and resonance effects which, as we demonstrate in this work, are not only significant but may dominate certain transitions and hence their collision *rates*. Since DW results are still extensively used in spectral modeling, these limitations to the accuracy should be noted.

The dense KLn resonance enhancement makes a large contribution to the effective collision strengths at low temperatures. Radiation damping (RD) effects are important for the KLn resonance structure, because the large E1 transition rate of $A=8.87\times 10^{12}\ {\rm s}^{-1}$ from $1s2p\ ^1P_1^{\rm o}$ occurs in this energy region so the Rydberg resonance series, $1s2p\ n\ell$, converging from below onto $1s2p\ ^1P_1^{\rm o}$ are damped out. Also, there are some interesting features appearing in the KLn

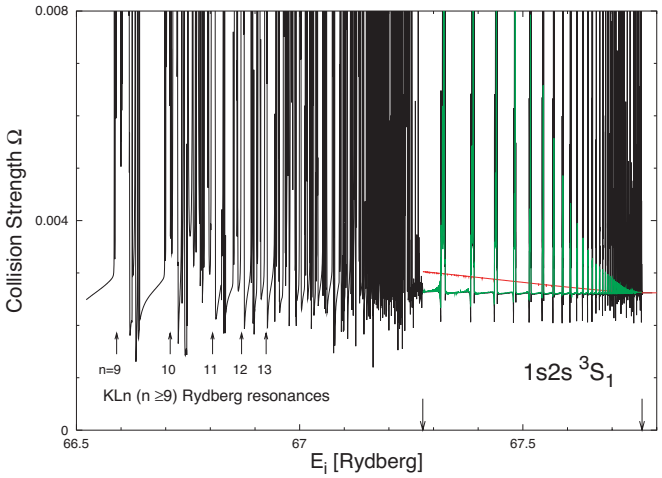

FIG. 2. (Color) An expansion of collision strength Ω from $n=5$ DRM calculations with detailed resonance structures as a function of incident electron energy E_i up to $n=2$ target threshold for M1 transition $1s^2\ ^1S_0-1s2s\ ^3S_1$. The black curve shows collision strengths without the inclusion of radiation damping (RD) effects, and the red curve (with Gaĭlitis average) and the green curve (without Gaĭlitis average) with the inclusion of RD effects. See text and Fig. 1 for notation.

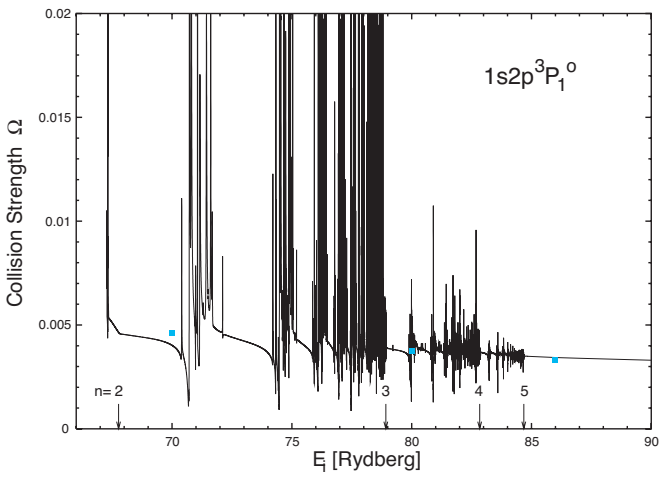

FIG. 3. (Color) Collision strength Ω from $n=5$ DRM calculations with detailed resonance structures as a function of incident electron energy E_i for E1 and IC transition $1s^2\ ^1S_0-1s2p\ ^3P_1^o$. The green squares are our RDW values [16]. See text and Fig. 1 for notation and more discussions.

resonance complexes. In order to show this more clearly, in Fig. 2 we expand a portion of the KL*n* resonance structures in Fig. 1. We also identify the first few members of the KL*n* resonance complexes converging onto four $n=2$ target thresholds denoted by a downward black arrow at ≈67.27 Ry. The RD effect on the Rydberg resonances converging onto the $1s2p\ ^1P_1^o$ target threshold, marked by adownward black arrow at 67.76 Ry, is discussed below. The red (with Gaĭlitis average [24]) and green (without Gaĭlitis average) curves show the collision strengths when the RD effects are included, while the black curve shows the collision strengths when the RD effect is not included for the energy region where the RD effect is important. From the comparison between the black curve (without RD) and two color curves (with RD) we find that the Rydberg series of resonances converging onto $1s2p\ ^1P_1^o$ are almost damped out as we expected. The small resonance enhancement over the background shows the Gaĭlitis averaged collision strengths [24] over the damped resonances (the red curve). The Gaĭlitis averaged collision strength patterns appear in the red curve for the energy region around 67.30 Ry because in our calculation with RD effects we averaged the collision strengths in the high ν-energy region (ν is the effective quantum defect number) when $\nu \geq 10$ [25–27]. The KLL through KL*n* ($n<8$) doubly excited states fall below the ionization potential of Ne VIII(IP=17.573 Ry=239.10 eV) and thus they make no contributions to the Rydberg resonance series. We also identify the KL*n* Rydberg series of resonances for $n=9-13$ according to quantum defect theory (QDT) [25]. We note that the labels identify only the location of the majority of the resonance states. For example, a small portion of high-lying levels in the $n=9$ resonance complex may appear in the location of the $n=10$ resonance complex. High n members of the Rydberg series of resonances could be further identified if the figure were enlarged. These identifications have also been confirmed by our MCDF calculation.

Figures 3 and 4 show the collision strengths for the intercombination transitions y (E1; 1–4) and x (M2; 1–5). The present RDW values are also shown for background comparison. The backgrounds for both 1–4 (y) and 1–5 (x) transitions decrease vs E_i, indicating that y is still spin forbidden by nature in this low E_i energy range. The resonance features are similar to those in Fig. 1 except that the KL*n* Rydberg resonance series almost disappears again because of the RD effect.

Figure 5 shows the collision strengths vs E_i for transition E1 (1–7) (the w line in the x-ray spectra notation) which is both optically allowed and spin allowed. Line w has the largest cross sections among the transitions from the ground state

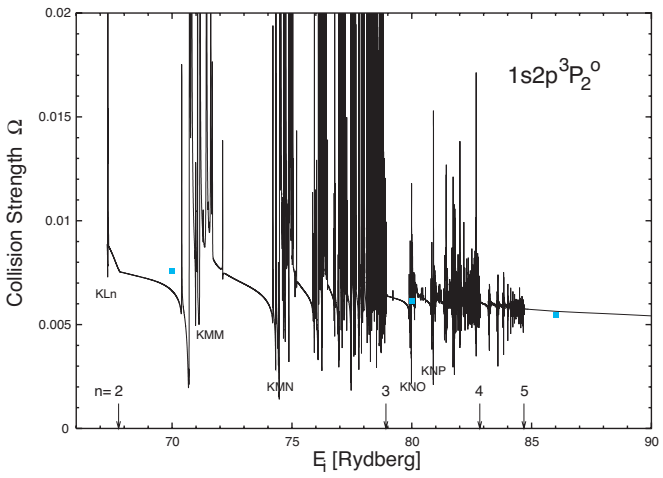

FIG. 4. (Color) Collision strength Ω from $n=5$ DRM calculations with detailed resonance structures as a function of incident electron energy E_i for M2 transition $1s^2\ ^1S_0-1s2p\ ^3P_2^o$. The green squares are our RDW values [16]. See text and Fig. 1 for notation and more discussions.

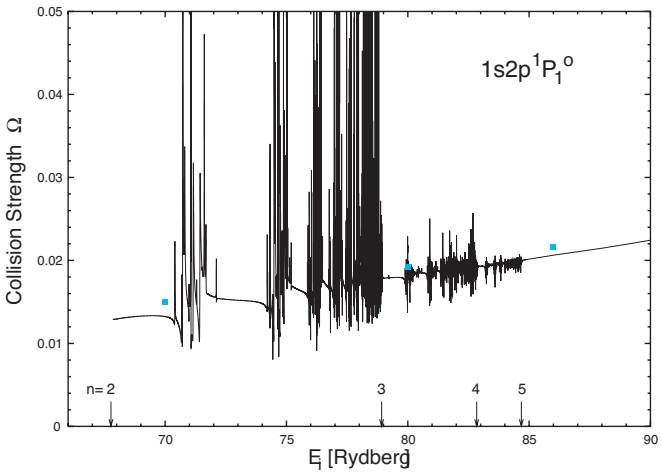

FIG. 5. (Color) Collision strength Ω from $n=5$ DRM calculations with detailed resonance structures as a function of incident electron energy E_i for E1 transition $1s^2\ ^1S_0-1s2p\ ^1P_1^o$ (dipole-allowed and spin-allowed). The green squares are our RDW values [16]. See text and Fig. 1 for notation and more discussions.

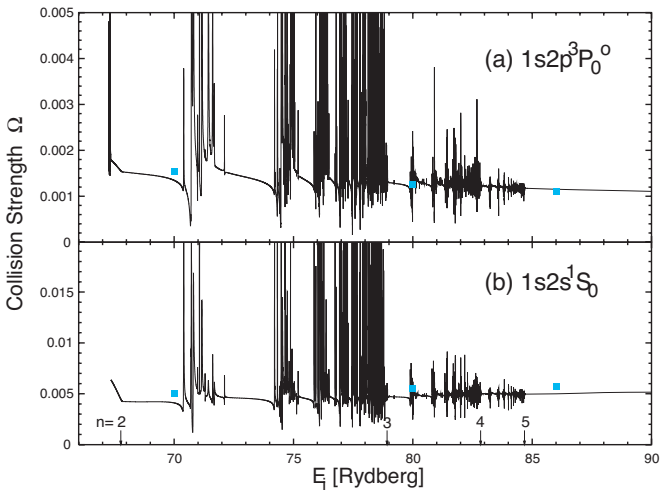

FIG. 6. (Color) Collision strength Ω from $n=5$ DRM calculations with detailed resonance structures as a function of incident electron energy E_i for monopole transitions (a) $1s^2\ ^1S_0-1s2p\ ^3P_0^o$ and (b) $1s^2\ ^1S_0-1s2s\ ^1S_0$. The green squares are our RDW values [16]. See text and Fig. 1 for notation.

in Ne IX emission or absorption spectra. The squares indicate the background RDW results.

Two main features are apparent: (i) Significant $n=3$ resonances appear even though this is the strongest E1 transition. This feature is important in comparing the relative line intensity measured in EBIT experiments, and in obtaining correct effective collision strengths under different electron velocity distributions (e.g., Gaussian and Maxwellian). (ii) The background of the DRM collision strengths is lower than that of the RDW results. This is due to channel coupling, in which the redistribution of electron flux over a larger number of thresholds reduces the background. Although this effect amounts to only a few percent difference in the w line background collision strength, it is very large compared to the background collision strengths in other transitions. Thus the flux redistribution away from w leads to a significant increase in other weaker transitions.

2. The monopole transitions

Monopole $(J=0-0)$ collisional excitation is of some interest, since radiation cannot excite such transitions. Figures 6(a) and 6(b) show the monopole collision strengths from the ground state to levels $3(1s2p\ ^3P_0^o)$ and $6(1s2s\ ^1S_0)$, respectively. The RDW values differ barely from the DRM background for the transition 1–3, however, the RDW values are higher than the background of the DRM results for the transition 1–6. This is an interesting feature similar to the transition 1–7 discussed in the preceding subsection, again due to the redistribution of electron flux among different channels. This is special because the transition 1–6 is a relatively small transition in contrast to the strong E1 transition 1–7. Normally channel coupling effects reduce the background of strong transitions and raise the background of weak transitions. Figure 6(b) indicates that this is one of the exceptions. We found a similar case in the previous Fe XVII calculation for the monopole transition from the ground state to $2p^53p\ ^1S_0$. Further study may be needed to confirm these results, although this is primarily of academic interest rather than for spectroscopic applications.

3. Transitions between excited levels

In Fig. 7, we show the collision strengths for transitions from the first excited state (level 2) to the other five higher $n=2$ levels. Transitions in Figs. 7(a)–7(c) are of E1 type with very large cross sections but without strong resonance enhancements as expected. The intercombination excitations $(S=0\rightarrow 1)$ in Figs. 7(d) and 7(e) have relatively small direct cross sections but relatively strong resonance patterns. The

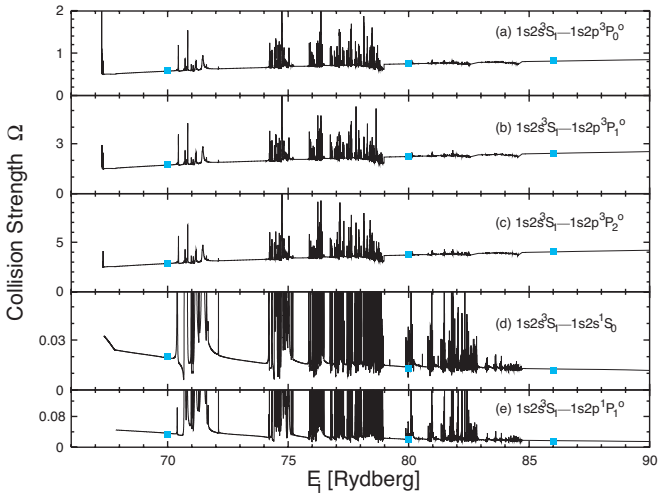

FIG. 7. (Color) Collision strength Ω from $n=5$ DRM calculations with detailed resonance structures as a function of incident electron energy E_i for transitions from the first excited state $^3S_1$ to the other five $n=2$ excited states. The green squares are our RDW values [16]. See text and Fig. 1 for notation and more discussions.

TABLE III. Comparison of collision strengths in Ne IX among the present DRM calculation (first row for each transition), the present RDW calculation (second row), and previous RM calculation (third row) [10] for five incident electron energies E_i above the highest 49CC target energy threshold. The index i and j label the levels involved in the transition from levels i to j (see Table I).

		E_i (Ry)				
i	j	90	100	110	120	130
1	2	1.87×10^{-3}	1.66×10^{-3}	1.54×10^{-3}	1.40×10^{-3}	1.21×10^{-3}
		1.87×10^{-3}	1.65×10^{-3}	1.46×10^{-3}	1.31×10^{-3}	1.18×10^{-3}
1	3	1.11×10^{-3}	9.41×10^{-3}	8.11×10^{-4}	7.21×10^{-4}	6.38×10^{-4}
		1.03×10^{-3}	8.67×10^{-4}	7.35×10^{-4}	6.31×10^{-4}	5.46×10^{-4}
1	4	3.31×10^{-3}	2.81×10^{-3}	2.43×10^{-3}	2.16×10^{-3}	1.91×10^{-3}
		3.10×10^{-3}	2.60×10^{-3}	2.21×10^{-3}	1.90×10^{-3}	1.65×10^{-3}
						1.68×10^{-3}
1	5	5.42×10^{-3}	4.61×10^{-3}	3.97×10^{-3}	3.52×10^{-3}	3.12×10^{-3}
		5.08×10^{-3}	4.25×10^{-3}	3.60×10^{-3}	3.09×10^{-3}	2.67×10^{-3}
						2.78×10^{-3}
1	6	5.17×10^{-3}	5.49×10^{-3}	5.95×10^{-3}	6.35×10^{-3}	6.45×10^{-3}
		5.87×10^{-3}	6.17×10^{-3}	6.43×10^{-3}	6.65×10^{-3}	6.84×10^{-3}
						6.56×10^{-3}
1	7	2.24×10^{-2}	2.63×10^{-2}	2.97×10^{-2}	3.30×10^{-2}	3.68×10^{-2}
		2.31×10^{-2}	2.68×10^{-2}	3.03×10^{-2}	3.35×10^{-2}	3.66×10^{-2}
						3.55×10^{-2}

transition 1–2 is of M1 type and level 2 is a metastable state. Competition between radiative decay of level 2 to the ground state (via the slow M1 transition) and collisional excitation to the $^3P^o$ levels is the basis of the well-known $R=i/f$ density diagnostic [28].

D. Comparison of collision strengths

In Table III, we compare the present DRM calculation, the present RDW calculation, and the previous RM calculation [10] of collision strengths for transitions from the ground state to the first six excited states at five E_i's between 90–130 Ry, all of which are above the 49CC highest threshold and the 87.9 Ry ionization potential of Ne IX. Large differences are found for some transitions, some well above 10%. For the transition 1–6, our RDW results are about 15% higher than the DRM results, and the previous RM results. For the transition 1–4 (y line), our DRM is 16% and 14% higher than the RDW and the previous RM results, respectively. For the transition 1–5 (x line), our DRM results are 17% and 12% higher than the RDW and the previous RM results, respectively. For the transition 1–3, our DRM results are 17% higher than our RDW results. These large differences may be due to the sensitivity of forbidden or intercombination transitions to channel coupling and resonance effects. For the transition 1–7, all the calculations are in good agreement to within a few percent as expected for a strong E1 transition. For the transition 1–2, our DRM and RDW results are in good agreement to within a few percent. There appear to be some typographical errors for the transitions 1–2 and 1–3 in [10], so they are not included in Table III.

E. Comparison of effective collision strengths

In Table IV, we compare the Maxwellian averaged effective collision strengths between the present DRM calculations and previous RM calculations [10] and previous DW calculations [8,9]. Although RD effects are included in our calculation of effective collision strengths in Ne IX, they are generally small when the collision strengths are convolved with a broad Maxwellian distribution, because they may appear to be important on resonance structures for a very narrow range of collision energies (see Sec. IV C 1). This point has also been shown by previous CC calculations [10]. At 10 MK, we reach the same conclusion as that in [10], i.e., all the results are in good agreement to within 5% except for some transitions in [8]. At 2 MK, the differences becomes larger between the present DRM calculations and previous RM calculations: 8% for the transition 1–2 and 7% for 1–7. At 0.4 MK, there are large differences up to 24% for the transition 1–6 and 20% for 1–2. We believe there is a typographical error in [10] for the effective collision strengths of the transition 1–7 at 2 MK, so this datum is not included in our comparison in Table IV.

F. *G* ratios

Significant resonance enhancement of the collision strengths of forbidden and intercombination transitions has been noted before (e.g. [15,17,19]) and demonstrated for Ne IX in this work. This directly enhances the rate coefficients which, in turn, affect the line intensities and ratios. The rate coefficients were obtained by averaging the collision strengths over a Maxwellian velocity distribution thought to prevail in most astrophysical plasmas.

To determine the overall effect of these enhancements, we calculated the G ratio using two different approaches using the APEC code [5]. First, we determined the Ne IX line intensities using a 49-level collisional-radiative (CR) model that

TABLE IV. Comparison of Maxwellian averaged effective collision strengths in Ne IX between the present DRM calculation (first row for each transition), and a previous RM calculation in [10] (second row), previous DW calculations in [9] (third row), and in [8] (fourth row) for five electron temperatures T. The index i and j label the levels involved in the transition from levels i to j (see Table I).

		T				
i	j	0.4 MK	1 MK	2 MK	4 MK	10 MK
1	2	6.53×10^{-3}	4.68×10^{-3}	3.64×10^{-3}	2.79×10^{-3}	1.83×10^{-3}
		7.85×10^{-3}		3.93×10^{-3}		1.88×10^{-3}
		3.04×10^{-3}		2.89×10^{-3}		1.65×10^{-3}
		6.79×10^{-3}		5.11×10^{-3}		2.30×10^{-3}
1	3	1.67×10^{-3}	1.62×10^{-3}	1.47×10^{-3}	1.24×10^{-3}	8.66×10^{-4}
1	4	5.00×10^{-3}	4.85×10^{-3}	4.39×10^{-3}	3.69×10^{-3}	2.61×10^{-3}
1	5	8.20×10^{-3}	7.98×10^{-3}	7.22×10^{-3}	6.07×10^{-3}	4.28×10^{-3}
1	6	4.79×10^{-3}	4.97×10^{-3}	5.11×10^{-3}	5.37×10^{-3}	6.05×10^{-3}
		5.95×10^{-3}		5.49×10^{-3}		6.07×10^{-3}
		5.04×10^{-3}		5.43×10^{-3}		6.23×10^{-3}
		4.98×10^{-3}		5.45×10^{-3}		6.22×10^{-3}
1	7	1.45×10^{-2}	1.63×10^{-2}	1.88×10^{-2}	2.33×10^{-2}	3.45×10^{-2}
		1.42×10^{-2}				3.33×10^{-2}
		1.51×10^{-2}		1.92×10^{-2}		3.33×10^{-2}
		1.27×10^{-2}		1.70×10^{-2}		3.24×10^{-2}
2	3	5.69×10^{-1}	6.30×10^{-1}	7.09×10^{-1}	8.00×10^{-1}	9.42×10^{-1}
2	4	1.71	1.91	2.12	2.40	2.82
2	5	2.84	3.18	3.53	3.99	4.69
2	6	3.02×10^{-2}	3.04×10^{-2}	2.57×10^{-2}	1.96×10^{-2}	1.25×10^{-2}
		3.29×10^{-2}		2.67×10^{-2}		1.29×10^{-2}
		2.90×10^{-2}		2.58×10^{-2}		1.21×10^{-2}
2	7	6.56×10^{-2}	6.65×10^{-2}	5.32×10^{-2}	3.68×10^{-2}	1.99×10^{-2}
		6.56×10^{-2}		5.27×10^{-2}		1.91×10^{-2}
		6.28×10^{-2}	5.11×10^{-2}		1.91×10^{-2}	

included transitions within Ne IX only. The inputs to the CR model are from our present large-scale MCDF atomic structure calculations and the Dirac R-matrix calculation, together with other atomic data in the database APED [5]. Results are shown in Table V for electron density $n_e=10^{12}$ cm^{-3}, but the differences are minor for a range of n_e between $n_e=10^8$ and 10^{13} cm^{-3}. These calculations bracket the physical conditions applicable to the EBIT experimental measurements ($n_e\simeq10^{12}-5\times10^{12}$ cm^{-3}) [3]. Table V shows that our results agree well with the experimental data, while a similar calculation done using the data in ATOMDB v1.3 [5], which uses the calculations of [9,29],has systematically low results.

Note that the G ratio calculated above is somewhat idealized as it does not include contributions from unresolved

TABLE V. G ratio comparison for both the Ne IX only CR (collisional-radiative) model at 10^{12} cm^{-3} (comparable to the EBIT experimental measurements) and the multi-ion CR model with dielectronic and radiative recombination (DR and RR) processes in the low-density limit (comparable to the Capella observation). The estimated uncertainty in EBIT measurements is 8% [3].

	CR including Ne IX only			Full CR with DR and RR		
T/K	This Work	ATOMDB v1.3 [5]	EBIT [3]	This Work	ATOMDB v1.3 [5]	Capella [6]
1e6	1.32	1.08	1.35	1.41	1.10	
2e6	1.02	0.85	1.08	1.07	0.87	
3e6	0.85	0.71	0.90	0.90	0.76	
4e6	0.72	0.61	0.77	0.80	0.68	0.93 ± 0.09
6e6	0.55	0.48	0.59	0.68	0.60	
1e7	0.37	0.32	0.39	0.57	0.52	

satellite lines, recombination of Ne *x* ions, or inner shell ionization of Ne VIII (this creates $1s2s\ ^3S_1$) [30]. For comparison, we also calculated the *G* ratio using a more realistic multi-ion approach which included dielectronic and radiative recombination into the ground and excited states of Ne IX. In this case we assumed the plasma was in collisional ionization equilibrium using the ion population calculations of [31], and used the dielectronic and recombination rates used in ATOMDB v1.3. Some results are also shown in Table V. The detailed and complete model calculations of $G=(i+f)/r$ and $R=i/f$ ratios will be reported elsewhere [32].

V. CONCLUSIONS

We have carried out a comprehensive and elaborate 49CC DRM calculation, hitherto the most detailed, for the electron impact excitation of Ne IX. Prominent resonances appear in the 49CC calculations over the entire energy range below the 49CC highest target threshold, depending on the type of transitions. These resonances may considerably enhance the effective collision strengths for several important transitions. From comparisons of the present DRM and RDW results, the background collision strengths of some transitions are also demonstrated to be affected due to interchannel coupling and subsequent redistribution of flux among a larger number of channels in the 49CC case.

Comparison with a previous RM calculation shows large differences between the two calculations at low-to-medium temperatures. The difference can reach up to 20% or more for some transitions. At high temperatures, the agreement is generally good.

The diagnostically important *G* ratio calculated with the APEC plasma code using inputs from the present calculation of relativistic atomic structure and EIE collision strengths is in good agreement with the EBIT measurements to within 8%. This is an indication of the accuracy of the present atomic calculation.

ACKNOWLEDGMENTS

This work was supported by NSF through a grant to the Institute for Theoretical Atomic, Molecular and Optical Physics at Harvard University and Smithsonian Astrophysical Observatory and by a Chandra X-Ray Observatory theory grant. N.S.B. and B.J.W. were supported by NASA Contract No. NAS8-39073 to the Chandra X-Ray Center. All the computational work was carried out at the cluster in the Computer Facility at Harvard-Smithsonian CfA.

[1] D. L. McKenzie and P. B. Landecker, Astrophys. J. **259**, 372 (1982).
[2] F. P. Keenan, D. L. McKenzie, S. M. McCann, and A. E. Kingston, Astrophys. J. **318**, 926 (1987).
[3] B. J. Wargelin, Ph.D. thesis, LLNL, 1993 (unpublished).
[4] I. H. Coffey, R. Barnsley, F. P. Keenan, and N. J. Peacock, J. Phys. B **27**, 1011 (1994).
[5] R. K. Smith, N. S. Brickhouse, D. A. Liedahl, and J. C. Raymond, Astrophys. J. Lett. **556**, L91 (2001).
[6] J.-U. Ness, N. S. Brickhouse, J. J. Drake, and D. P. Huenemoerder, Astrophys. J. **598**, 1277 (2003).
[7] M. Matranga, M. Barbera, A. Maggio, G. Peres, S. Serio, E. Takács, E. H. Silver, J. D. Gillaspy, H. W. Schnopper, J. M. Laming, J. Beeman, E. E. Haller, and N. Madden, Nucl. Instrum. Methods Phys. Res. B **205**, 244 (2003).
[8] A. K. Pradhan, D. W. Norcross, and D. G. Hummer, Phys. Rev. A **23**, 619 (1981).
[9] H. L. Zhang and D. H. Sampson, Astrophys. J., Suppl. Ser. **63**, 487 (1987).
[10] M. A. Bautista, J. Phys. B **36**, 1503 (2003).
[11] F. Delahaye, A. K. Pradhan, and C. J. Zeippen, e-print astro-ph/0603482 (2006).
[12] S. Ait-Tahar, I. P. Grant, and P. H. Norrington, Phys. Rev. A **54**, 3984 (1996); P. H. Norrington and I. P. Grant, DARC codes.
[13] F. A. Parpia, C. F. Fischer, and I. P. Grant, Comput. Phys. Commun. **94**, 249 (1996).
[14] G. X. Chen, (unpublished).
[15] G. X. Chen, K. Kirby, and N. S. Brickhouse, Phys. Rev. A **73**, 052708 (2006); G. X. Chen, K. Kirby, E. Silver, N. S. Brickhouse, J. D. Gillaspy, J. N. Tan, J. Pomeroy, and J. M. Laming, Phys. Rev. Lett. **97**, 143201 (2006).
[16] G. X. Chen, Phys. Rev. A **53**, 3227 (1996).
[17] G. X. Chen, A. K. Pradhan, and W. B. Eissner, J. Phys. B **36**, 453 (2003).
[18] A. Burgess and J. A. Tully, Astron. Astrophys. **254**, 436 (1992).
[19] G. X. Chen and A. K. Pradhan, Phys. Rev. Lett. **89**, 013202 (2002).
[20] B. J. Wargelin, P. Beiersdorfer, and S. M. Kahn, Phys. Rev. Lett. **71**, 2196 (1993).
[21] E. Träbert, P. Beiersdorfer, G. V. Brown, A. J. Smith, S. B. Utter, M. F. Gu, and D. W. Savin, Phys. Rev. A **60**, 2034 (1999).
[22] http://physics.nist.gov/PhysRefData/.
[23] W. R. Johnson, I. M. Savukov, U. I. Safronova, and A. Dalgarno, Astrophys. J., Suppl. Ser. **141**, 543 (2002);W. R. Johnson, D. R. Plante, and J. Sapierstein, Adv. At., Mol., Opt. Phys. **35**, 255 (1995).
[24] M. Gaĭlitis, Sov. Phys. JETP **17**, 1328 (1963).
[25] M. J. Seaton, Rep. Prog. Phys. **46**, 167 (1983).
[26] R. H. Bell and M. J. Seaton, J. Phys. B **18**, 1589 (1985).
[27] A. K. Pradhan and M. J. Seaton, J. Phys. B **18**, 1631 (1985).
[28] A. H. Gabriel and C. Jordan, Mon. Not. R. Astron. Soc. **145**, 241 (1969).
[29] D. H. Sampson, S. J. Goett, and R. E. H. Clark, At. Data Nucl. Data Tables **29**, 467 (1983).
[30] B. J. Wargelin, S. M. Kahn, and P. Beiersdorfer, Phys. Rev. A **63**, 022710 (2001).
[31] P. Mazzotta, G. Mazzitelli, S. Colafrancesco, and N. Vittorio, Astrophys. J., Suppl. Ser. **133**, 403 (1998).
[32] R. K. Smith, G. X. Chen, and N. S. Brickhouse.